Simulation of Paraequilibrium Growth in Multicomponent Systems

G. GHOSH and G.B. OLSON

A methodology to simulate paraequilibrium (PE) growth in multicomponent systems using the DIC-TRA (Diffusion-Controlled Transformation) software is presented. For any given multicomponent system containing substitutional and interstitial elements, the basic approach is to define a hypothetical element Z, whose thermodynamic and mobility parameters are expressed in terms of the weighted average (with respect to site fraction) of the thermodynamic parameters and mobilities of the substitutional alloying elements. This procedure facilitates the calculation of PE phase diagrams and the PE growth simulations directly in the Thermo-Calc and DICTRA software, respectively. The results of two distinct case studies in multicomponent alloys are presented. In the first example, we simulate the isothermal growth of PE cementite in an Fe-C-Co-Cr-Mo-Ni secondary hardening steel during tempering. This is of practical importance in modeling the carbide precipitation kinetics during secondary hardening. In the second example, we have presented the results of PE ferrite growth during continuous cooling from an intercritical temperature in an Fe-Al-C-Mn-Si low-alloy steel. This is of importance to the design of triple-phase steels containing an austenite that has optimum stability, to facilitate stress-induced transformation under dynamic loading. The results of both simulations are in good accord with experimental results. The model calculations do not consider any resistive or dissipative forces, such as the interfacial energy, strain energy, or solute drag, and, as a result, the interface velocities represent an upper limit under the available chemical driving force.

I. INTRODUCTION

THE kinetic theories of diffusional phase transformations in alloys containing both substitutional and interstitial elements are well developed.[1-7] An important feature of various kinetic models is the assumption of local equilibrium of local equilibrium at the interface. Depending on the interface velocity during transformation, it is convenient to classify the kinetics into two distinct modes, as follows.

(1) Partitioning local equilibrium is characterized by a low interface velocity while maintaining local equilibrium at the interface. This condition is also referred to as orthoequilibrium (OE). Generally, OE occurs at low supersaturation, and its kinetics is governed by the slow-diffusing species (substitutional elements). For example, the thermodynamic condition for OE between ferrite (α) and cementite (θ) in ultrahigh-strength (UHS) steels is given by

$$\mu_i^\alpha = \mu_i^\theta \qquad [1]$$

where μ_i is the chemical potential of element i (representing C, Co, Cr, Fe, Ni, Mo, V, and W).

(2) Paraequilibrium (PE) is a kinetically constrained equilibrium, in which the diffusivity of the substitutional species is negligible compared to that of interstitial species. Hultgren argued that if carbon diffuses appreciably faster than the substitutional alloying elements, then the growing phase inherits the substitutional alloy contents. Furthermore, if the substitutional alloying elements are not allowed to partition,

their individual chemical potentials have no physical relevance and, thus, the thermodynamic behavior of these elements can be expressed by one hypothetical element, Z. Then, PE is defined by a uniform carbon potential and a uniform site fraction of substitutional elements across the transforming interface. For example, in the case of the α/θ transformation, the thermodynamic conditions for PE are given by

$$\mu_C^\alpha = \mu_C^\theta \qquad [2a]$$

$$y_j^\alpha = y_j^\theta \qquad [2b]$$

$$\mu_Z^\alpha \left(\equiv \sum y_j \, \mu_j^\alpha\right) = \mu_Z^\theta \left(\equiv \sum y_j \, \mu_j^\theta\right) \qquad [2c]$$

where the y_j terms are the site fractions of substitutional element j (representing Co, Cr, Fe, Ni, Mo, V, and W). For a system containing both substitutional (j) and interstitial elements (C or N), the site fractions are related to the ordinary mole fractions (x) as follows.

$$y_j = \frac{x_j}{1 - x_C - x_N} \qquad [3a]$$

$$y_{C \text{ or } N} = \frac{p}{q} \frac{x_{C \text{ or } N}}{1 - x_C - x_N} \qquad [3b]$$

According to the two-sublattice model[8] used here to express the Gibbs energies, $p = 1$ and $q = 3$ for ferrite, and $p = q = 1$ for austenite.

The schematic concentration profiles across the transforming interface for the aforementioned two distinct modes are shown in Figure 1. The PE growth mode can also be conceived as the complete solute trapping[9] in the substitutional sublattice. The central idea behind solute trapping is that when the interface velocity is greater than the diffusional

G. GHOSH, Research Assistant Professor, and G.B. OLSON, Wilson-Cook Professor of Engineering Design, are with the Department of Materials Science and Engineering, Robert R. McCormick School of Engineering and Applied Science, Northwestern University, Evanston, IL 60208-3108.
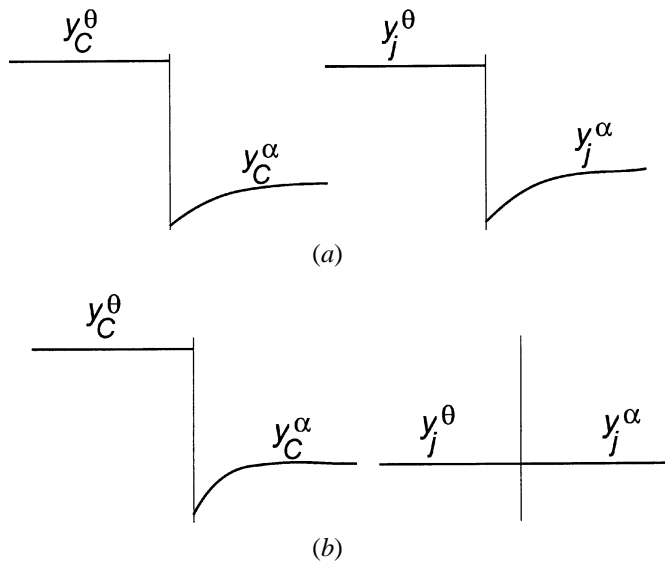
Fig. 1—Schematic composition profiles across the transforming interface associated with (*a*) OE and (*b*) PE phase transformation involving ferrite (α) and cementite (θ). The *X*-axis represents distance and the *Y*-axis represents concentration. The cementite is the growing phase.

Table I. Composition (in Weight Percent) of Model UHS Steels and Power Plant Steels Used for Thermodynamic Calculations

Alloy	Fe	C	Co	Cr	Mo	Ni	V
GRI-C1	bal	0.25	30.00	5.00	0.50	8.00	0.06
C3B	bal	0.16	28.00	5.00	2.75	3.100	—
AF1410*	bal	0.16	14.25	2.10	1.05	10.15	—
AerMet100*	bal	0.24	13.50	3.00	1.00	11.00	—
SRG1	bal	0.23	14.17	0.06	3.96	10.24	—
SRG2	bal	0.24	15.99	0.02	4.03	4.96	—
SRG3	bal	0.24	16.08	0.71	2.82	4.97	—
SRG4	bal	0.24	16.06	1.40	1.52	4.98	—
FeCrMoC1**	bal	0.15	—	2.25	1.00	—	—
FeCrMoC2**	bal	0.40	—	2.25	1.00	—	—

*Commercial alloys.
**Ref. 19.

velocity, the solute atoms will be trapped behind the advancing interface. The extent of solute trapping is determined by the magnitude of the interface velocity relative to the diffusional velocity. The former should be much greater than the latter for complete solute trapping. An intermediate case (incomplete solute trapping) between OE and PE is often referred to as no-partition local equilibrium (NPLE). It is characterized by a high interface velocity while maintaining local equilibrium at the interface. The NPLE is proposed to occur at high supersaturation, with its kinetics governed by the fast-diffusing species (interstitial elements). The NPLE is further characterized by the presence of a steep concentration profile (or a diffusion spike) ahead of the advancing interface.

The authors' research activities include experimental[10–16] and theoretical studies[15,16] of the kinetics of carbide precipitation during secondary hardening of UHS steels. The experimental techniques employed are transmission electron microscopy (TEM) and small-angle neutron scattering measurements, to determine the particle size, number density, and volume fraction, and atom probe field-ion microscopy (APFIM) and high-resolution analytical electron microscopy (AEM) to determine the composition. Our theoretical studies of carbide precipitation kinetics employ advanced computational thermodynamics and kinetics software, such as Thermo-Calc[17] and DICTRA[18] (Diffusion Controlled Transformation), respectively. Some of the model UHS steels used in our studies and two power-plant steels that also undergo secondary hardening[19] are listed in Table I.

The tracer diffusivities (D_T) of C, Co, Cr, Mo, and Ni[20–23] in pure α-Fe and their predicted chemical diffusivities (D_{Ch}) in the model alloy SRG3 at a standard tempering temperature of 783 K are listed in Table II. The chemical diffusivities are calculated using the mobility database[24] in conjunction with the DICTRA software. The differences between D_T and D_{Ch} are due to thermodynamic factors.

Nonetheless, it may be noted that the substitutional elements diffuse about nine to eleven orders of magnitude slower than carbon.

Due to the previous kinetic argument, the precipitation of cementite during bainitic transformation or tempering of martensite provides an ideal opportunity to study PE phase transformation. This is why the composition of cementite with respect to substitutional elements in bainitic or tempered martensite has been investigated many times. Baker and Nutting[25] used the energy-dispersive X-ray (EDX) analysis in extraction replica and showed that the substitutional solute content in cementite after short tempering times at 673 and 773 K in an Fe-2.25Cr-1Mo-0.15C steel was similar to that of the bulk alloy composition. Chance and Ridley[26] investigated the chromium partitioning of cementite in a bainitic microstructure formed at 823 K in an Fe-1.41Cr-0.81C steel using EDX analysis of extraction replicas. They found very little evidence for chromium partitioning. Babu *et al.*[27] used the APFIM technique to study the chemistry of cementite that formed during tempering of an Fe-1.84C-3.84Si-2.95Mn steel in the temperature range from 623 to 773 K. Their results showed that the substitutional alloy content in cementite was the same as that in the starting alloy at the early stage of tempering thus confirming cementite growth by the PE mode. This is despite the fact that the equilibrium solubility of Si in cementite is practically zero. Furthermore, they did not observe any compositional spike at the cementite/martensite interface and found that the PE state of cementite moves toward the NPLE state with continued tempering. Thomson and Miller[19] also used the APFIM technique and studied the chemistry of cementite in Fe-2.25Cr-1Mo-0.15C and Fe-2.25Cr-1Mo-0.4C steels after tempering for various times at 623 and 723 K. They also did not observe any evidence of partitioning of Cr and Mo between cementite and martensite, even after tempering up to 40 hours at 623 K, nor did they observe any compositional spike at the cementite/martensite interface. Very recently, Ghosh *et al.*[14] reported the composition of cementite that formed during tempering of an Fe-0.247C-16.08Co-0.71Cr-2.28Mo-4.97Ni alloy at 783 K for up to 15 minutes. They carried out high-resolution EDX analysis of the extracted particles in AEM and found that the substitutional alloy content in cementite was the same as that in the starting

Table II. The Tracer Diffusivities (D_T) of C, Co, Cr, Ni, and Mo in α-Fe and Their Chemical Diffusivities (D_{Ch}) in the Experimental Alloy SRG3 at 783 K

Element	D_T at 783 K, m^2/s	D_T^j/D_T^C	D_{Ch} at 783 K, m^2/s	D_{Ch}^j/D_{Ch}^C
C	4.979×10^{-12}	—	1.301×10^{-12}	—
Co	3.052×10^{-21}	6.130×10^{-10}	8.468×10^{-23}	6.509×10^{-11}
Cr	1.580×10^{-20}	3.173×10^{-9}	4.597×10^{-22}	3.533×10^{-10}
Mo	5.830×10^{-21}	1.171×10^{-9}	1.456×10^{-22}	1.119×10^{-10}
Ni	5.597×10^{-21}	1.124×10^{-9}	1.276×10^{-21}	9.808×10^{-10}

alloy, thus confirming the PE nature of the precipitated cementite.

To understand the growth kinetics under the PE transformation mode, the purpose of this report is to propose a methodology to simulate PE growth kinetics using the DICTRA software. While the current version of Thermo-Calc allows PE calculations of multicomponent systems in conjunction with the PARROT module, the current version of DICTRA does not allow PE growth simulation directly, although it is expected that such calculations will be implemented in a future version of DICTRA. Using the proposed methodology, we will present the results of two case studies. The first case is the simulation of the growth of PE cementite that forms at the early stages of tempering of Fe-C-Co-Cr-Mo-Ni martensitic steels. The second case is the simulation of the growth of PE ferrite in an Fe-C-Mn-Si low-alloy steel during continuous cooling from an intercritical temperature.

II. MULTICOMPONENT THERMODYNAMICS AND KINETICS MODELS

Thermo-Calc[17] is a multipurpose software system used to calculate thermodynamic properties of phases and heterophase equilibria in multicomponent systems. DICTRA[18] is a general software package used to simulate diffusion-controlled transformations in multicomponent systems involving multiple phases, but in one dimension. It is important to note that DICTRA uses Thermo-Calc to calculate the thermodynamic factor of the phases to convert mobility into diffusivity and also to compute the local equilibrium between the phases. In other words, to use DICTRA successfully, a complete thermodynamic description of the participating phase(s) is needed first, and, then, the kinetic description of the corresponding phase(s) is needed.

As an example, to simulate PE-α/PE-θ growth in Fe-C-Co-Cr-Mo-Ni alloys, the basic approach is schematically shown in Figure 2. Since the substitutional alloying elements are not allowed to partition during PE-α/PE-θ transformation, we define a hypothetical element Z, whose thermodynamic properties in the phase ψ are derived from the thermodynamic properties of the substitutional alloying elements in that phase. By a similar argument, we derive the mobility of Z in phase ψ from the mobilities of the substitutional alloying elements in that phase. In the following text, we discuss this procedure in detail for multicomponent systems.

A. Paraequilibrium Thermodynamics in Multicomponent Systems

The Thermo-Calc software employs the sublattice model[28] to express the Gibbs energies of phases in multicomponent systems. Besides the excess Gibbs energies of mixing, the model also accounts for the Gibbs energy contributions due to magnetic and atomic ordering. For a multicomponent ferrite phase (α), the sublattice representation is $(x_1, x_2, x_3, \ldots)$ (C, Va)$_3$, where the x_j terms are the substitutional elements and C and Va are carbon and the vacancy interstitials, respectively. Then, the molar Gibbs energy of α is given by

$$
\begin{aligned}
G_m^\alpha = {} & y_C \sum y_j G_{j:C}^{0,\alpha} + y_{Va} \sum y_j G_{j:Va}^{0,\alpha} \\
& + RT(\sum y_j \ln y_j + 3y_C \ln y_C + 3y_{Va} \ln y_{Va}) \quad [4] \\
& + G_m^{xs,\alpha} + G_m^{mag,\alpha}
\end{aligned}
$$

where the y_j terms are the site fractions of the element j, and y_C and y_{Va} are the site fractions of carbon and vacancies, respectively. The parameters $G_{j:C}^{0,\alpha}$ and $G_{j:Va}^{0,\alpha}$ represent the molar Gibbs energy of the α phase when the first sublattice is fully occupied by the element j and the second sublattice is fully occupied by either C or Va, respectively. In Eq. [4], the first two terms correspond to the Gibbs energies due to mechanical mixture; the third term is the ideal Gibbs energy of mixing; the fourth term is the excess Gibbs energy of mixing; which is expressed as a Redlich–Kister–Muggianu polynomial;[29] the fifth term is the Gibbs energy contribution due to magnetic ordering; R is the universal gas constant; and T is the absolute temperature. Equation [4] can be expanded and rewritten in the following form:

$$
\begin{aligned}
G_m^\alpha = {} & y_C \left(\sum y_j G_{j:C}^{0,\alpha} + RT \sum y_j \ln y_j \right. \\
& + \sum_{j \neq k} \sum y_j y_k (L_{j,k:C}^{0,\alpha} + (y_j - y_k) L_{j,k:C}^{1,\alpha} + \ldots) \\
& \left. + \sum_{j \neq k \neq l} \sum \sum y_j y_k y_l \, L_{j,k,l:C}^{0,\alpha} \right) \\
& + y_{Va} \left(\sum y_j G_{j:Va}^{0,\alpha} + RT \sum y_j \ln y_j \right. \\
& + \sum_{j \neq k} \sum y_j y_k (L_{j,k:Va}^{0,\alpha} + (y_j - y_k) L_{j,k:Va}^{1,\alpha} + \ldots) \quad [5] \\
& \left. + \sum_{j \neq k \neq l} \sum \sum y_j y_k y_l \, L_{j,k,l:Va}^{0,\alpha} \right) \\
& + y_C y_{Va} \left(\sum y_j L_{j:C,Va}^{0,\alpha} + \sum_{j \neq k} \sum y_j y_k L_{j,k:C,Va}^{0,\alpha} + \ldots \right) \\
& + y_C y_{Va} (y_C - y_{Va}) \left(\sum y_j L_{j:C,Va}^{1,\alpha} \right. \\
& \left. + \sum_{j \neq k} \sum y_j y_k (y_j - y_k) \, L_{j,k:C,Va}^{1,\alpha} + \ldots \right)
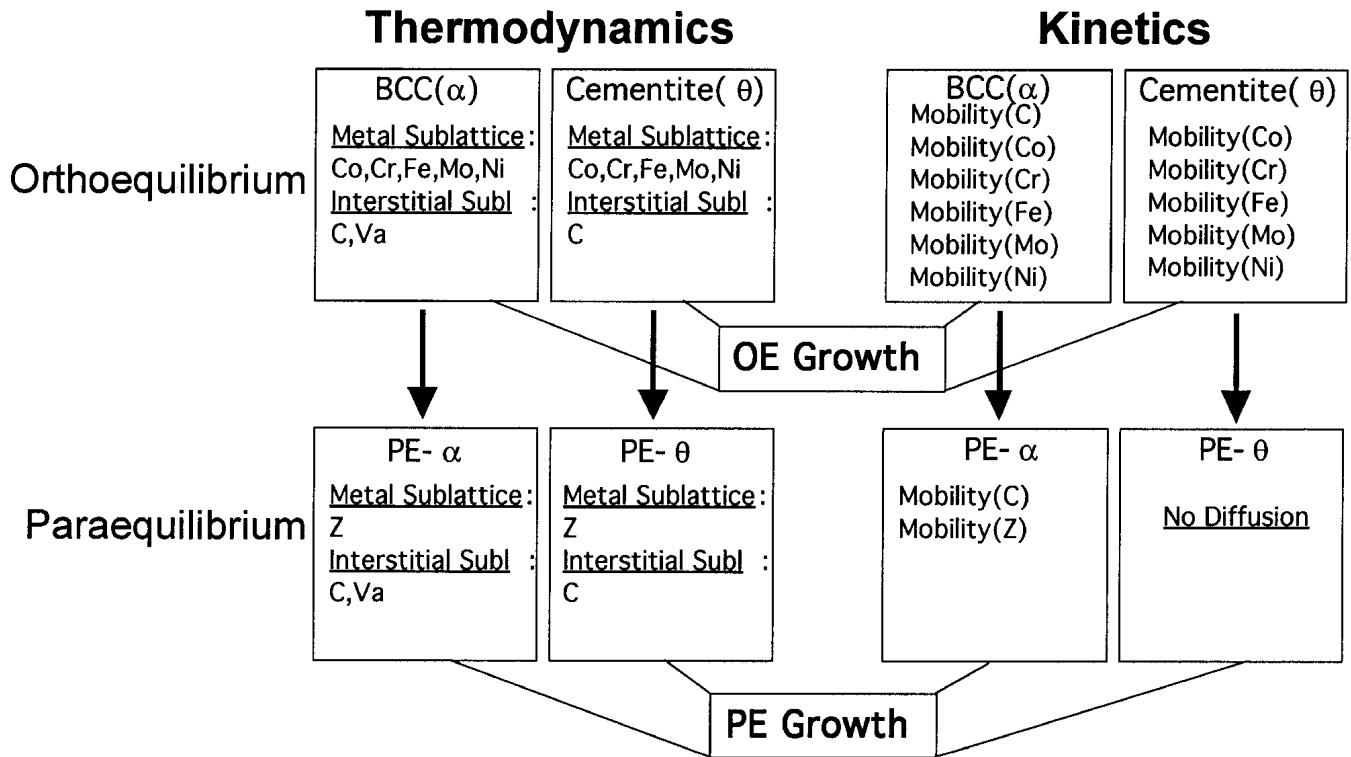\end{aligned}
$$

Thermodynamics

Fig. 2—The relationship between the thermodynamic and kinetic parameters under OE and PE conditions. Also, the schematic methodology to simulate PE growth.

$$+ 3RT(y_C \ln y_C + y_{Va} \ln y_{Va}) + G_m^{mag,\alpha}$$

where $L_{j,k:C}^{0,\alpha}$, $L_{j,k:Va}^{0,\alpha}$, $L_{j,k,l:C}^{0,\alpha}$, $L_{j,k,l:Va}^{0,\alpha}$, *etc.*, are the interaction parameters to account for the excess Gibbs energy of mixing. These quantities are derived by fitting various experimental information, such as the heat of mixing, activity, phase-diagram boundaries, *etc.* According to the model proposed by Hillert and Jarl,[30] the quantity $G_m^{mag,\alpha}$ in Eq. [5] is expressed as

$$G_m^{mag,\alpha} = RT \ln (\beta^\alpha + 1) f(\tau^\alpha) \qquad [6]$$

where β^α is the average Bohr magneton of α and $\tau^\alpha = T/T_c^\alpha$, with T_c^α being the Curie temperature of α. The function of $f(\tau^\alpha)$ is expressed as truncated polynomials.[30] Like solution thermodynamics, the composition dependencies of β^α and T_c^α in a multicomponent system are also expressed by Redlich–Kister polynomials:

$$\beta^\alpha = y_C \left(\sum y_j \beta_{j:C}^{0,\alpha} + \sum\sum_{j\neq k} y_j y_k (\beta_{j,k:C}^{0,\alpha} \right.$$
$$+ (y_j - y_k) \beta_{j,k:C}^{1,\alpha} + \ldots)$$
$$+ \sum\sum\sum_{j\neq k\neq l} y_j y_k y_l \, \beta_{j,k,l:C}^{0,\alpha})$$
$$+ y_{Va} \left(\sum y_j \beta_{j:Va}^{0,\alpha} + \sum\sum_{j\neq k} y_j y_k (\beta_{j,k:Va}^{0,\alpha} \right.$$
$$+ (y_j - y_k) \beta_{j,k:Va}^{1,\alpha} + \ldots) \qquad [7]$$
$$+ \sum\sum\sum_{j\neq k\neq l} y_j y_k y_l \, \beta_{j,k,l:Va}^{0,\alpha})$$
$$+ y_C y_{Va} \left(\sum y_j \beta_{j:C,Va}^{0,\alpha} + \sum\sum_{j\neq k} y_j y_k \beta_{j,k:C,Va}^{0,\alpha} + \ldots \right)$$

$$+ y_C y_{Va} (y_C - y_{Va}) \left(\sum y_j \beta_{j:C,Va}^{1,\alpha} \right.$$
$$+ \sum\sum_{j\neq k} y_j y_k (y_j - y_k) \beta_{j,k:C,Va}^{1,\alpha} + \ldots)$$

$$T_c^\alpha = y_C \left(\sum y_j T_{cj:C}^{0,\alpha} + \sum\sum y_j y_k (T_{cj,k:C}^{0,\alpha} \right.$$
$$+ (y_j - y_k) T_{cj,k:C}^{1,\alpha} + \ldots)$$
$$+ \sum\sum\sum_{j\neq k\neq l} y_j y_k y_l T_{cj,k,l:C}^{0,\alpha}) \qquad [8]$$
$$+ y_{Va} \left(\sum y_j T_{cj:Va}^{0,\alpha} + \sum\sum_{j\neq k} y_j y_k (T_{cj,k:Va}^{0,\alpha} \right.$$
$$+ (y_j - y_k) T_{cj,k:Va}^{1,\alpha} + \ldots)$$
$$+ \sum\sum\sum_{j\neq k\neq l} y_j y_k y_l T_{cj,k,l:Va}^{0,\alpha})$$
$$+ y_C y_{Va} \left(\sum y_j T_{cj:C,Va}^{0,\alpha} + \sum\sum_{j\neq k} y_j y_k T_{cj,k:C,Va}^{0,\alpha} + \ldots \right)$$
$$+ y_C y_{Va} (y_C - y_{Va}) \left(\sum y_j T_{cj:C,Va}^{1,\alpha} \right.$$
$$+ \sum\sum_{j\neq k} y_j y_k (y_j - y_k) T_{cj,k:C,Va}^{1,\alpha} + \ldots)$$

As an example, $\beta_{j:C}^{0,\alpha}$ is the Bohr magneton parameter of α when one sublattice is fully occupied by the element j and other sublattice is fully occupied by carbon. The interaction parameters $\beta_{j,k:C}^{0,\alpha}$, $\beta_{j,k:Va}^{0,\alpha}$, $\beta_{j,k,l:C}^{0,\alpha}$, $\beta_{j,k,l:Va}^{0,\alpha}$, *etc.* are derived from the experimental composition dependence of the magnetic moment, and so are the interaction parameters to describe T_c^α.

Under PE conditions, the sublattice description for the α

phase (PE-α) is (Z) (C, Va)$_3$, where Z is a hypothetical element. Then, the molar Gibbs energy of PE-α is expressed as

$$G_m^{\text{PE-}\alpha} = y_C G_{Z:C}^{0,\text{PE-}\alpha} + y_{Va} G_{Z:Va}^{0,\text{PE-}\alpha} + y_C y_{Va} L_{Z:C,Va}^{0,\text{PE-}\alpha}$$

$$+ y_C y_{Va}(y_C - y_{Va}) L_{Z:C,Va}^{1,\text{PE-}\alpha} \qquad [9]$$

$$+ 3RT(y_C \ln y_C + y_{Va} \ln y_{Va}) + G_m^{\text{mag,PE-}\alpha}$$

$$G_m^{\text{mag,PE-}\alpha} = RT \ln (\beta^{\text{PE-}\alpha} + 1)f(\tau^{\text{PE-}\alpha}) \qquad [10]$$

where $\beta^{\text{PE-}\alpha}$ is the average Bohr magneton of PE-α and $\tau^{\text{PE-}\alpha} = T/T_c^{\text{PE-}\alpha}$, with $T_c^{\text{PE-}\alpha}$ being the Curie temperature of PE-α. The composition dependence of $\beta^{\text{PE-}\alpha}$ and $T_c^{\text{PE-}\alpha}$ are expressed as

$$\beta^{\text{PE-}\alpha} = y_C \beta_{Z:C}^{0,\text{PE-}\alpha} + y_{Va} \beta_{Z:Va}^{0,\text{PE-}\alpha}$$

$$+ y_C y_{Va}\beta_{Z:C,Va}^{0,\text{PE-}\alpha} + y_C y_{Va}(y_C - y_{Va}) \beta_{Z:C,Va}^{1,\text{PE-}\alpha} + \ldots) \qquad [11]$$

$$T_c^{\text{PE-}\alpha} = y_C T_{cZ:C}^{0,\text{PE-}\alpha} + y_{Va} T_{cZ:Va}^{0,\text{PE-}\alpha}$$

$$+ y_C y_{Va} T_{cZ:C,Va}^{0,\text{PE-}\alpha} + y_C y_{Va}(y_C - y_{Va})T_{cZ:C,Va}^{1,\text{PE-}\alpha} + \ldots) \qquad [12]$$

By comparing Eq. [5] with Eq. [9], it may be seen that the thermodynamic parameters of PE-α can be very easily calculated from those of the α phase. For example, the term multiplied by y_C in Eq. [5] is equivalent to $G_{Z:C}^{0,\text{PE-}\alpha}$, in Eq. [9], the term multiplied by y_{Va} in Eq. [5] is equivalent to $G_{Z:Va}^{0,\text{PE-}\alpha}$ in Eq. [9], and so on. Similarly, by comparing Eqs. [7] and [8] with Eqs. [11] and [12], the parameters describing the composition dependence of the Bohr magneton moment and Curie temperature for PE-α can be calculated from those of the α phase. However, it is not necessary that these cumbersome calculations be performed manually on a case-by-case basis. Rather, for any given multicomponent system, it is possible to rewrite the Gibbs-energy data file of the α phase in such a manner that, for any given composition, all parameters describing $G_m^{\text{PE-}\alpha}$, $\beta^{\text{PE-}\alpha}$, and $T_c^{\text{PE-}\alpha}$ will be automatically calculated by the Thermo-Calc software by knowing only the site fraction of the substitutional elements in that system. In an analogous manner, the molar Gibbs energy of PE cementite (PE-θ) can also be expressed in terms of the thermodynamic quantities of the cementite phase provided in the SSOL database of the Thermo-Calc software systems.

The thermodynamic driving force is a very fundamental quantity in understanding any phase-transformation kinetics and mechanisms. Using Eq. [9] for PE-α and an analogous equation for PE-θ, we can construct their molar Gibbs-energy curves as a function of carbon content. Then, the driving force for nucleation of PE-θ (ΔG^N) is given by the parallel tangent construction, as shown schematically in Figure 3. Then ΔG^N is given by

$$\Delta G^N = (\mu_Z^{N,\text{PE-}\theta} - \mu_Z^{N,\text{PE-}\alpha}) x_Z^{N,\text{PE-}\theta}$$

$$+ (\mu_C^{N,\text{PE-}\theta} - \mu_C^{N,\text{PE-}\alpha}) x_C^{N,\text{PE-}\theta} \qquad [13]$$

where $x_i^{N,\varphi}$ is the mole fraction of element i in the critical nucleus and $\mu_i^{N,\varphi}$ is the corresponding chemical potential. Under OE conditions, the driving force for nucleation is given by

$$\Delta G_i^N = (\boldsymbol{\mu}_i^{N,\theta} - \boldsymbol{\mu}_i^{N,\alpha})\mathbf{x}_i^{N,\theta} \qquad [14]$$

where $\boldsymbol{\mu}_i$ (equal to $\mu_1, \mu_2, \ldots, \mu_n$) and $\mathbf{x}_i$ (equal to $x_1, x_2, \ldots, x_n$) are vectors.
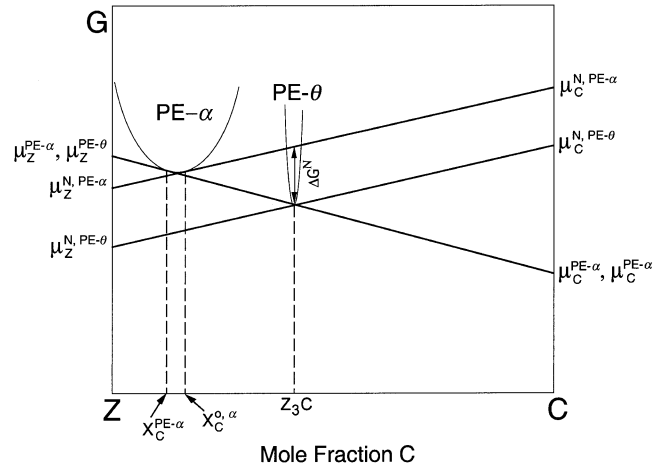

Fig. 3—Schematic Gibbs energy *vs* composition plot for the paraequilibrium ferrite (PE-α) and paraequilibrium cementite (PE-θ) phases showing the parallel tangent construction to determine the driving force for nucleation (ΔG^N) of PE-θ from PE-α. $X_C^{o,\alpha}$ is the initial carbon content in the alloy and $X_C^{\text{PE-}\alpha}$ is the carbon content in PE-α after complete precipitation of PE-θ. The μ is the chemical potential.

The thermodynamic driving forces for the nucleation of competing carbides during tempering of model alloys, listed in Table I, were calculated. These include PE-θ and OE-θ, coherent M$_2$C, incoherent M$_2$C, M$_6$C, M$_{23}$C$_6$, and M$_7$C$_3$. The SGTE thermochemical database[31] for multicomponent systems in conjunction with the Thermo-Calc software[32] is used in the present thermodynamic analysis. Campbell[16] modeled the coherency effects on the nucleation and coarsening of the M$_2$C carbides by considering the composition-dependent elastic energy and the composition-independent interfacial energy, which were added to the molar Gibbs energy of the M$_2$C phase. An implicit assumption was that the elastic energy is independent of the volume fraction, which is not unreasonable at a low volume fraction of the coherent precipitates. Thus, the molar Gibbs energy of coherent M$_2$C is given by

$$G_m^{\text{Coherent M}_2\text{C}} = G_m^{\text{Chemical}} + G_m^{\text{Elastic}} + G_m^{\text{Interfacial}} \qquad [15]$$

The elastic strain energy is a function of the ferrite and M$_2$C lattice parameters and the ferrite and M$_2$C elastic moduli. The linear-elastic strain energy associated with an inhomogeneous inclusion, as a function of lattice parameters and shear moduli, has been determined by Liarng.[33] For the alloy M$_2$C carbides, the compositional dependence of the lattice parameters and shear moduli has been investigated by Knepfler.[34] Combining the work of Liarng and Knepfler, the composition dependence of the elastic strain energy was expressed by Redlich–Kister polynomials.[29]

The results of the driving-force calculations in model alloys are listed in Table III. Since PE is a constrained equilibrium, the driving force for the nucleation of PE-θ is much smaller than that of OE-θ. Also, Cr has a very strong effect in determining the difference in the driving force between PE-θ and OE-θ. When the Cr content is negligible, as is the case for model alloys SRG1 and SRG2, this difference is rather small. The chemical driving force for the nucleation of M$_{23}$C$_6$ is also very sensitive to the Cr content in the alloy. Due to strain-energy effects, the driving force for the nucleation of coherent M$_2$C is smaller than that of

Table III. The Calculated Chemical Driving Forces for the Nucleation of Competing Carbides from a Fully Supersaturated Ferrite in Model UHS Steels and Power Plant Steels

	Chemical Driving Force (J/mol) for Nucleation						
Alloy	Cementite (PE)	Cementite (OE)	M_2C (Coherent)	M_2C (Incoherent)	M_6C	$M_{23}C_6$	M_7C_3
GRI-C1*	6590	20,327	22,504	26,511	11,006	20,115	25,312
C3B*	5104	19,406	21,618	27,538	15,694	20,183	23,709
AF1410*	6427	14,729	18,432	25,573	13,753	16,018	19,613
AerMet100*	7011	15,914	19,277	25,566	13,459	16,938	20,836
SRG1*	6980	8731	22,196	31,643	18,579	9025	24,396
SRG2*	6597	8297	21,715	31,168	18,452	8418	23,954
SRG3*	6666	11,750	20,472	29,690	17,176	13,969	22,424
SRG4*	6754	14,219	18,997	27,178	14,975	15,746	19,853
FeCrMoC1**	8633	20,323	24,377	32,015	19,531	21,596	25,178
FeCrMoC2**	9937	19,551	24,218	31,817	18,597	20,577	24,703

*UHS steels at a tempering temperature of 783 K.
**Power plant steels at a tempering temperature of 623 K.

incoherent M_2C. Furthermore, among the competing carbides considered here, the driving force for the nucleation of PE-θ is the smallest; however, due to the kinetic advantage, it forms first during tempering.

B. *Paraequilibrium Kinetics in Multicomponent Systems*

To simulate PE growth using DICTRA, we will extend Hultgren's argument of the chemical potentials of substitutional elements under PE to include mobility. That is, if the substitutional elements do not partition during a diffusional phase transformation, their individual mobilities have no physical relevance, and, thus, these elements behave kinetically as if there were only one element.

The temporal profile of the diffusing species k in a multicomponent system is given by the Fick's first law in the mass-conservation form

$$\frac{\partial C_k}{\partial t} = -\mathbf{div}\,(J_k) \qquad [16]$$

where C_k is the concentration in moles per volume, and div denotes the divergence operator. The diffusional flux of the species k (J_k) in a multicomponent system is given by the Fick–Onsager law

$$J_k = -\sum_{j=1}^{n-1} D_{kj}^n \nabla C_j \qquad [17]$$

where D_{kj}^n are the diffusion coefficients. The summation is performed over an $(n-1)$ independent concentration, as the dependent nth component may be taken as the solvent. For a solid solution containing both substitutional and interstitial elements, Andersson and Ågren[35] proposed that the diffusion coefficients may be expressed, in a number fixed frame of reference, with respect to the substitutional elements,

$$D_{kj} = \sum_{i \in S} (\delta_{ik} - u_k) u_i M_i \frac{\partial \mu_i}{\partial u_j} + \sum_{i \notin S} \delta_{ik} u_i y_{Va} M_i \frac{\partial \mu_i}{\partial \nu_j} \qquad [18]$$

where $i \in S$ and $i \notin S$ denote that i is a substitutional or an interstitial element, respectively; δ_{ik} is the Kroneker delta; M_i is the atomic mobility of element i; the derivative of the chemical potential of the element i (μ_i) is calculated from thermodynamic description of the phase; and y_{Va} is the site

fraction of the vacant interstitial site. The concentration variable u_i is defined by

$$u_i = \frac{x_i}{\sum_{j \in S} x_j} \qquad [19]$$

where x_i is the ordinary mole fraction. The diffusion coefficients D_{kj}^n in Eq. [7] are related to the reduced diffusivity D_{kj}, also called the chemical diffusivity, in Eq. [18]:

$$D_{kj}^n = D_{kj} - D_{kn}, \text{ when } j \in S \qquad [20]$$

$$D_{kj}^n = D_{kj}, \text{ when } j \notin S \qquad [21]$$

Based on the absolute-reaction-rate-theory arguments, Andersson and Ågren[35] proposed that the mobility of an element i in the phase ψ (M_i^ψ) has a frequency factor ($M_i^{F,\psi}$) and an activation enthalpy factor ($M_i^{Q,\psi}$), and these are related by the expression

$$M_i^\psi = \frac{M_i^{F,\psi}}{RT} \exp\left(-\frac{M_i^{Q,\psi}}{RT}\right) \qquad [22]$$

Both $M_i^{F,\psi}$ and $M_i^{Q,\psi}$ are composition dependent. In the spirit of the CALPHAD approach, Andersson and Ågren[35] proposed that, in a multicomponent system, both $M_i^{F,\psi}$ and $M_i^{Q,\psi}$ be expressed with a linear combination of the values at each end point of the composition space and a Redlich–Kister–Muggianu polynomial. For the elements and phases of interest in this study, the $M_i^{F,\psi}$ and $M_i^{Q,\psi}$ parameters were obtained from the mobility database in conjunction with the DICTRA software.[24] From these quantities, we can derive the mobilities of C and the hypothetical element Z and can simulate PE growth. For example, the mobility of C under the PE condition can be expressed as

$$\Phi_C^{PE-\alpha} = y_C \Phi_{Z:C}^{0,PE-\alpha} + y_{Va} \Phi_{Z:Va}^{0,PE-\alpha}$$
$$= y_C \sum_{i \in S} y_i \Phi_{i:C}^{0,\alpha} + y_{Va} \sum_{i \in S} y_i \Phi_{i:Va}^{0,\alpha} \qquad [23]$$

where ϕ_i can be either M_i^F or M_i^Q. In other words, the mobility parameters for C under the PE condition are the weighted average, with respect to the site fraction of substitutional alloying elements. The quantities $\Phi_{i:C}^{0,\alpha}$, $\Phi_{i:Va}^{0,\alpha}$, *etc.*,

representing the mobility parameters of C, are readily available in the mobility database.[24] Similarly, the mobility of the hypothetical element Z under the PE condition can be expressed as

$$
\begin{aligned}
\Phi_Z^{PE-\alpha} &= y_C\Phi_{Z:C}^{0,PE-\alpha} + y_{Va}\Phi_{Z:Va}^{0,PE-\alpha} + y_C y_{Va}\Phi_{Z:Va}^{0,PE-\alpha} \\
&\quad + y_C y_{Va}(y_C - y_{Va})\Phi_{Z:CVa}^{1,PE-\alpha} \\
&= y_C \left(\sum_{i\in S} y_i\Phi_{i:C}^{0,\alpha} + \sum_{j\neq k\in S}\sum y_j y_k(\Phi_{j,k:C}^{0,\alpha}\right. \\
&\quad + (y_j - y_k)\Phi_{j,k:C}^{1,\alpha} + \ldots) \\
&\quad + \sum_{j\neq k\neq l\in S}\sum\sum (y_j y_k y_l\Phi_{j,k,l:C}^{0,\alpha} + \ldots) \\
&\quad + y_{Va}\left(\sum_{i\in S} y_i\Phi_{i:Va}^{0,\alpha} + \sum_{j\neq k\in S}\sum y_j y_k(\Phi_{j,k:Va}^{0,\alpha}\right. \qquad [24] \\
&\quad + (y_j - y_k)\Phi_{j,k:Va}^{1,\alpha} + \ldots) \\
&\quad + \sum_{j\neq k\neq l\in S}\sum\sum (y_j y_k y_l\Phi_{j,k,l:Va}^{0,\alpha} + \ldots) \\
&\quad + y_C y_{Va}[\sum_{j\neq k\in S}\sum y_j y_k\Phi_{j,k:C,Va}^{0,\alpha} + \ldots) \\
&\quad + \sum_{j\neq k\neq l\in S}\sum\sum (y_j y_k y_l\Phi_{j,k,l:C,Va}^{0,\alpha} + \ldots) \\
&\quad + y_C y_{Va}(y_C - y_{Va}) \left(\sum_{j\neq k\in S}\sum y_j y_k(y_j - y_k)\right. \\
&\quad \Phi_{j,k:C,Va}^{1,\alpha} + \ldots)
\end{aligned}
$$

Once again, the mobility parameters for Z can be derived by taking a weighted average of the corresponding parameters with respect to the site fraction of substitutional alloying elements. For the elements of interest here, the parameters $\Phi_{j,k:C}^{0,\alpha}$, $\Phi_{j,k:C}^{1,\alpha}$, $\Phi_{j,k:Va}^{0,\alpha}$, $\Phi_{j,k:Va}^{1,\alpha}$, *etc.*, are readily available in the mobility database.[24]

Under the α/θ OE condition, the moving velocity of the interface is given by the flux-balance equation

$$
\nu_\xi^{OE} = \frac{J_{Co}^{\xi\alpha} - J_{Co}^{\xi\theta}}{X_{Co}^{\xi\alpha} - X_{Co}^{\xi\theta}} = \frac{J_{Cr}^{\xi\alpha} - J_{Cr}^{\xi\theta}}{X_{Cr}^{\xi\alpha} - X_{Cr}^{\xi\theta}} = \frac{J_{Mo}^{\xi\alpha} - J_{Mo}^{\xi\theta}}{X_{Mo}^{\xi\alpha} - X_{Mo}^{\xi\theta}} = \ldots \qquad [25]
$$

where V_ξ^{OE} is the velocity of the interface; $X_{Co}^{\xi\alpha}$ and $X_{Co}^{\xi\theta}$ are the concentration of Co at the α- and θ-phase interface, respectively, $J_{Co}^{\xi\alpha}$ and $J_{Co}^{\xi\theta}$ are the corresponding diffusional fluxes, respectively; and so on.

III. RESULTS OF SIMULATIONS

A. *Case I: Growth of PE Cementite during Tempering*

Figures 4(a) and (b) show the bright-field TEM micrographs of the extracted cementite particles in the experimental alloy SRG3 after tempering at 783 K for 5 and 10 minutes, respectively. The cementite particles may be categorized as intra- and interlath types. It is believed that both intra- and interlath cementite particles nucleate heterogeneously, the former in the vicinity of dislocations within the martensite lath and the latter in the martensite lath boundaries. The interlath cementite particles precipitate as laths that have a high aspect ratio (length/width). The intralath particles are somewhat irregular in shape; nonetheless, they are characterized by their lengths and widths. Generally, the interlath cementite particles are smaller than the interlath cementite particles. Perhaps the intralath cementite particles formed
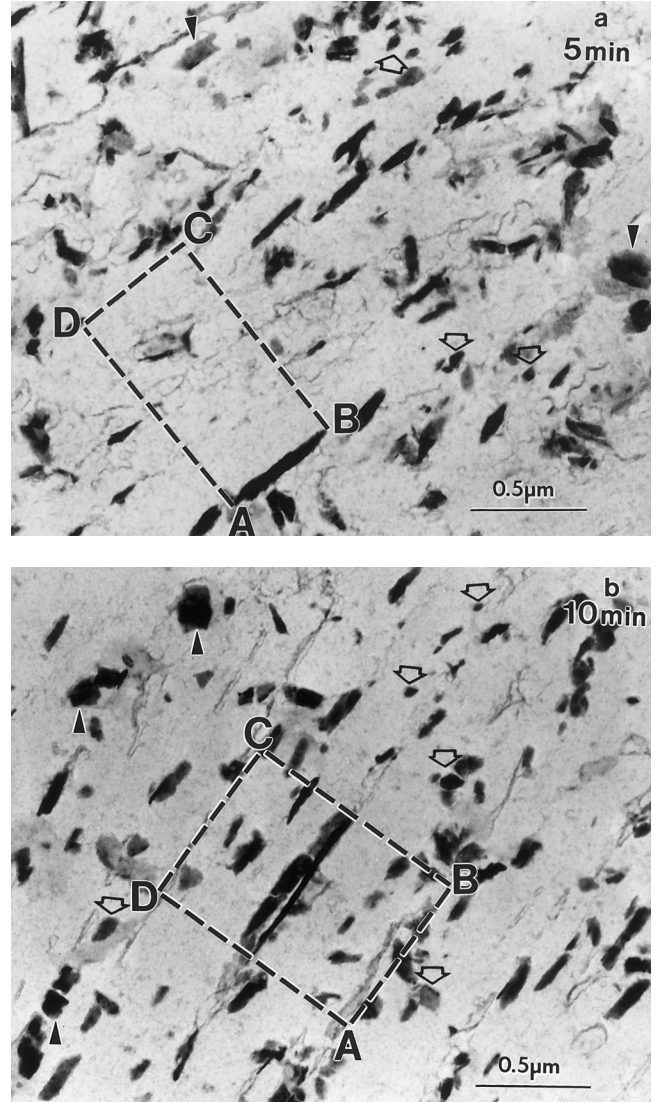

Fig. 4—Bright-field TEM micrographs of the PE-θ particles, in extraction replica, after tempering the model alloy SRG3 at 783 K: (*a*) for 5 min and (*b*) for 10 min. The cells ABCD in (a) and (b) correspond to those shown schematically in Figs. 5(a) and (b), respectively.

at a lower supersaturation compared to the initial supersaturation. Nonetheless, AEM characterization confirmed the PE nature of both types of cementite particles.

Following the methodology described in Section II, the Gibbs-energy data file and the mobility data file for the α and θ phases were rewritten in a rather generic manner for the Fe-C-Co-Cr-Mo-Ni system. Then, the simulation of PE-θ growth for any given composition in this system becomes very straightforward. Thin-foil examination of the lath martensitic microstructure shows that the laths are, in general, about 0.5-μm wide. This is also supported by the footprints of the lath boundaries in the extraction replica micrographs shown in Figures 4(a) and (b). Schematic representation of an interlath PE-θ particle is shown in Figures 5(a) and (b), which correspond to the experimental microstructures shown in Figures 4(a) and (b), respectively. From the mass-balance criterion alone, the growth of one PE-θ particle from one martensite lath of 1 μm in width (Figure 5(a)) is equivalent to the growth of one PE-θ particle at the interface of two
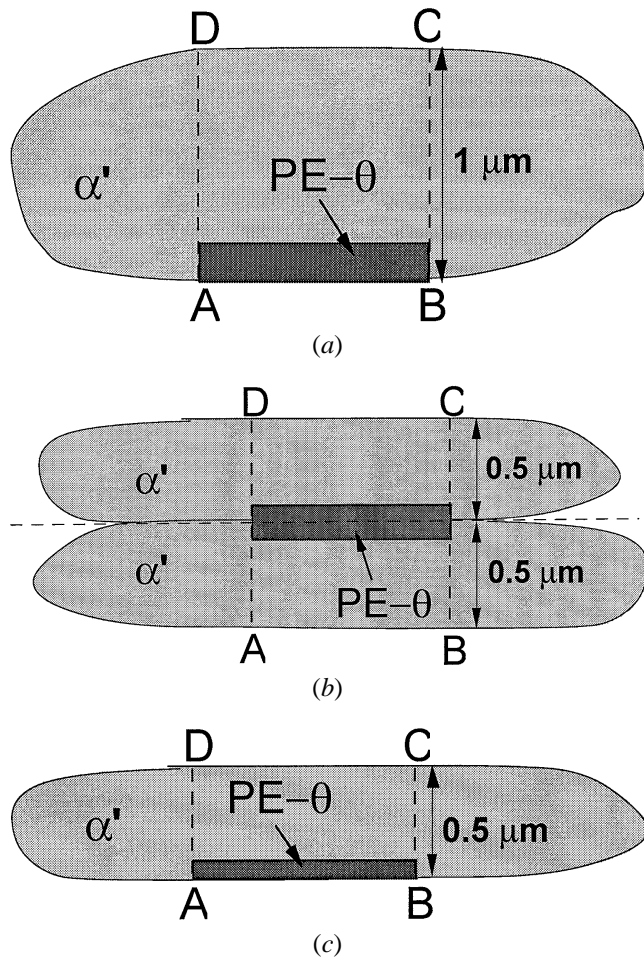
Fig. 5—(a) through (c) Simplified diffusion geometries to simulate the growth of paraequilibrium cementite (PE-θ) at the lath martensite (α') boundaries. From the mass balance consideration within the cell ABCD, the growth of one PE-θ particle in a lath of 1-μm width (shown in (a)) is equivalent to the growth of one PE-θ particle at the interface two laths of 0.5-μm width each (shown in (b)). Our DICTRA simulations correspond to the geometries in (a) and (c).

laths of 0.5 μm in width each (Figure 5(b)). We consider the growth of one interlath PE-θ particle at the boundary of two martensite laths, which is equivalent to a cell that has a linear dimension of 1 μm, as shown in Figure 5(a), and we also consider the growth of one interlath PE-θ particle at the boundary of one martensite lath, as shown in Figure 5(c). The choice of a flat geometry is consistent with the morphology of the interlath cementite particles shown in Figures 4(a) and (b). The governing mass-conservation and flux equations under the PE condition are

$$\frac{\partial C_C}{\partial_t} = -\mathbf{div}\,(J_C) \qquad [26]$$

$$J_C = -D_C \frac{\partial C_C}{\partial x} \qquad [27]$$

Then, the moving velocity of the PE-α/PE-θ interface is given by

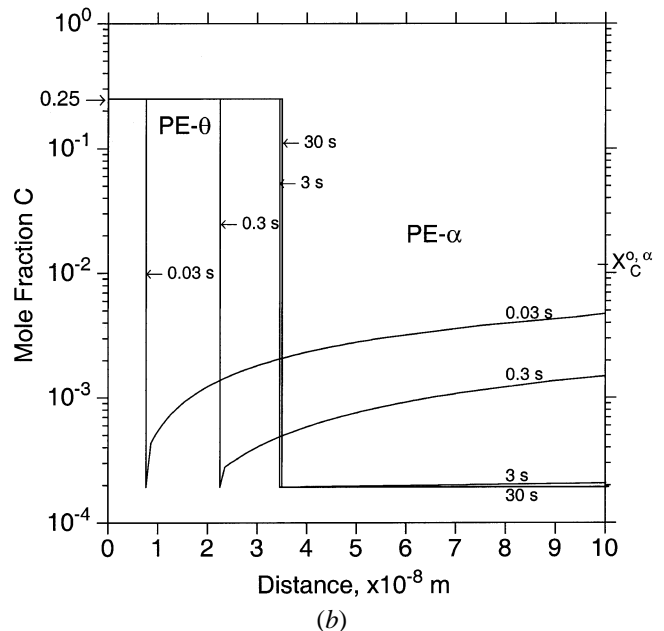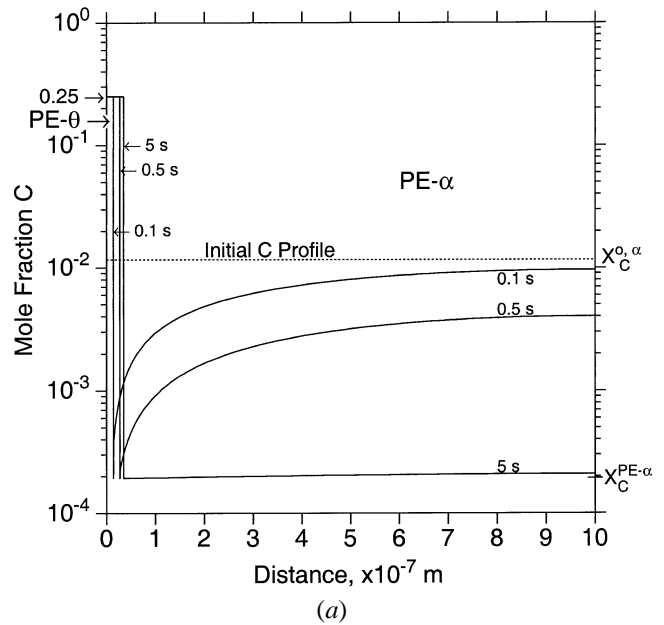$$\nu_\xi^{PE} = \frac{J_C^{\xi\alpha}}{X_C^{\xi\alpha} - 0.25} \qquad [28]$$

Fig. 6—The simulated paraequilibrium growth of PE-θ having a flat interface in an Fe-0.247C-16.08Co-0.71Cr-2.82Mo-4.97Ni alloy at 783 K as a function of time. (a) the carbon profile in the matrix (PE-α) and (b) an enlarged portion of (a). The Y-axis is in logarithmic scale to clearly show the carbon profile within PE-α. The initial carbon content and that after the completion of paraequilibrium growth (or transformation) are marked as $X_C^{0,\alpha}$ and $X_C^{PE-\alpha}$, respectively.

A fundamental assumption in the simulation is that the thermodynamic and kinetic parameters of the lath martensite phase are the same as those of the ferrite phase. A further simplification is that, even though the interlath PE-θ particles nucleate and grow at the lath boundaries, growth simulations are carried out by considering the lattice mobility in PE-α. Under the PE condition, the cementite phase is stoichiometric with respect to both Z and C; therefore, diffusion within PE-θ need not be considered.

Figures 6(a) and (b) show the growth of a PE-θ particle in an Fe-0.247C-16.05CO-0.71Cr-2.82Mo-4.97Ni alloy at

783 K as a function of time. Development of the C concentration profile with time in the PE-α matrix may be noted. The initial and final C contents (after complete growth of the PE-θ particle) are marked as $X_C^{0,\alpha}$ and $X_C^{PE-\alpha}$, respectively, in Figure 6(a). As shown in Figure 6(b), most of the growth of the PE-θ particle takes place within the first few seconds, and the extent of growth between 3 and 30 seconds is negligible. This implies that once the PE-θ particles have nucleated, their growth rate determined by C diffusion alone is rather fast. Based on the diffusion geometry shown in Figure 5(a), the PE-θ particle grows to about 35 nm. This is in very good agreement with the average thickness of 41 to 45 nm reported by Ghosh et al.[14] for the same alloy. A lower predicted thickness than the experimental value is justifiable from a mass-balance consideration alone, because in the real microstructure the PE-θ particles do not grow all along the interlath boundaries. It may also be noted that, after complete growth of the PE-θ particle, the C content in the matrix has decreased by more than two orders in magnitude. This causes about a 40 pct reduction in the driving force for the nucleation of the coherent M_2C phase that gives rise to secondary hardening.[14]

Figures 7(a) and (b) show the growth kinetics of PE-θ for a time period of 3 seconds, corresponding to the diffusion geometrics shown in Figures 5(a) and (c), respectively. It is seen that the initial parabolic kinetics law is the same in both cases. Also, in both cases, the initial parabolic kinetics continues up to about 50 pct of the transformation. This is despite the fact that the far-field supersaturation drops below the initial supersaturation even before 50 pct transformation, as shown by the C profile after 0.1 seconds in Figure 6(a). The initial parabolic growth kinetics is characterized by a time-independent rate constant, and the deviation from this behavior during the later stages of growth can be described by a time-dependent rate constant due to the rapid decrease in the driving force during the growth. The nonparabolic kinetics at the later stages is only an apparent effect, because the growth is volume-diffusion (of C) controlled during the entire time period.

The moving velocity of the PE-α/PE-θ interface for the two initial conditions in Figures 5(a) and (c) is shown in Figure 8. As expected, both initial conditions exhibit the same initial interface velocity. Furthermore, the growth velocity of the PE-θ particle in a lath 0.5-μm wide remains the same as that in a lath 1-μm wide until about 50 pct transformation occurs in the former, beyond which the interface velocities depart from each other. Initially, the interface velocity is very high because of the very high driving force. As the supersaturation of the matrix decreases during the growth of the PE-θ particle, the interface velocity also gradually decreases, and, finally, at the later stages of growth, the interface velocity drops precipitously. Based on the thickness measurements of the PE-θ particles between 5 and 10 minutes of tempering at 783 K, Ghosh et al.[14] reported that the average thickening rate is about 4×10^{-11} m/s. This is well within the range of predicted interface velocities at a comparable size scale during later stages of growth, as shown in Figure 8.

For the case in hand, a very strong dependence of interface velocity on the driving force suggests that, to measure the initial growth velocity of PE-θ, an in-situ technique with very good temporal resolution needs to be employed, and
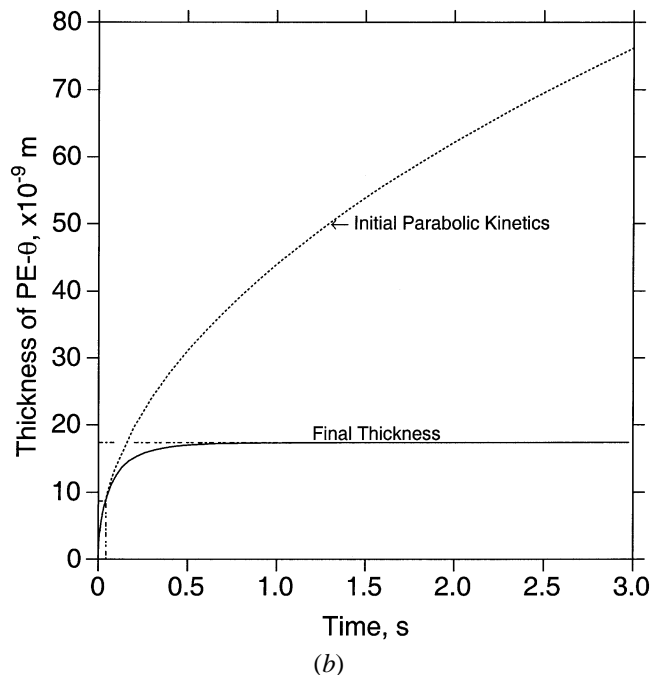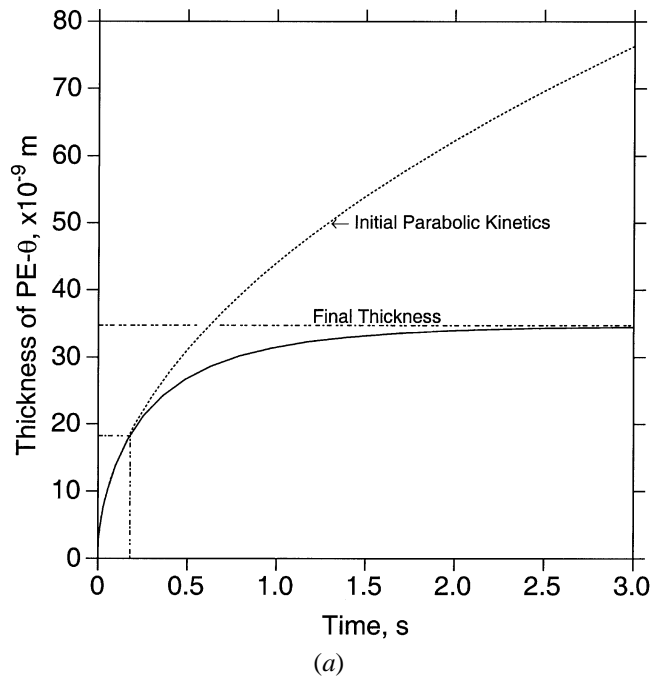

(a)

(b)

Fig. 7—The simulated paraequilibrium thickening kinetics of the PE-θ particle in an Fe-0.247C-16.08Co-0.71Cr-2.82Mo-4.97Ni alloy at 783 K for up to 3 s: (a) corresponds to the diffusion geometry in Fig. 5(a), and (b) corresponds to the diffusion geometry in Fig. 5(b). The dotted line shows the thickness of PE-θ if the initial parabolic kinetics would have continued for the entire time period.

it cannot be measured by ex-situ experiments. Ghosh et al.[14] estimated the growth velocity based on the average thickness of the PE-θ particles in extraction replicas. Even when one evaluates the growth velocity based on the maximum thickness of the PE-θ particle, either on a polished section of the specimen or in an extraction replica, it will always correspond to the late stages of growth kinetics. It is also possible that the thickening rate measured by Ghosh et al. corresponds to that of a coarsening process under PE. Even then, the

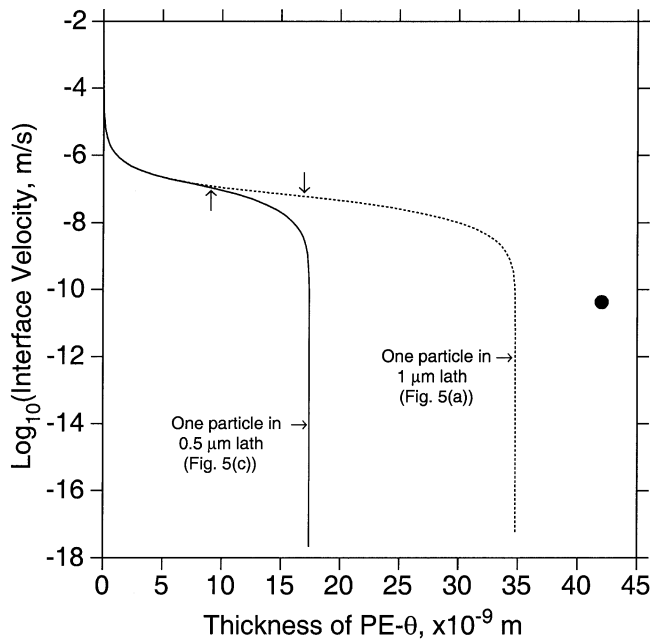Fig. 8—The PE-θ/PE-α interface velocity, in an Fe-0.247C-16.08Co-0.71Cr-2.82Mo-4.97Ni alloy at 783 K, as a function of the thickness of PE-θ. The solid circle corresponds to the growth rate estimated by Ghosh *et al.*[14] The vertical arrows indicate the interface velocities at 50 pct transformation.

Fig. 9—Schematic time-temperature processing diagram to design triple-phase microstructure in low alloy steels.

measured thickening rate is consistent with the predicted interface velocity, because the coarsening process is expected to occur at a much lower supersaturation compared to the initial supersaturation.

B. *Case II: Growth of PE Ferrite during Continuous Cooling*

The design of new triple-phase steels is of current interest in the automobile industry. The microstructure of triple-phase steels consists of ferrite, bainite, and austenite. The latter phase undergoes transformation to martensite during deformation, giving rise to the phenomenon called transformation-induced plasticity (TRIP). To exploit all advantages of the TRIP phenomenon, an optimum stability of the austenite phase, determined by its composition and size, is very crucial. A typical processing schedule to develop a triple-phase microstructure involves a short intercritical annealing (in the ferrite + austenite two-phase field) followed by rapid cooling to about 673 to 723 K, where it is held isothermally to induce bainite and then quenched to room temperature. The schematic time-temperature processing diagram for designing a triple-phase microstructure in low-alloy steels is shown in Figure 9. In low-alloy steels containing 1.5 mass pct Mn, Speich *et al.*[36] found that during short-term intercritical annealing, the kinetics of austenite formation is controlled by C diffusion. During this period, a PE is established between ferrite and austenite. During rapid cooling from the intercritical annealing temperature to about 673 K, ferrite grows into austenite while maintaining PE. The extent of this growth has a strong influence on the C content in the austenite, which, in turn, significantly influences the bainitic and the martensitic transformation kinetics.

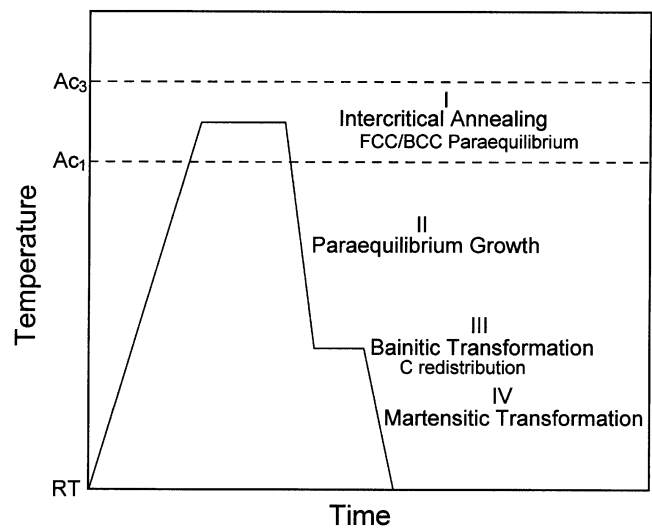Brandt[37] investigated the effect of the stability of retained austenite on the mechanical properties of Fe-0.05Al-0.26C-0.8 to 2.24Mn-1.52Si alloys. These steels were intercritically annealed at 1043 K followed by rapid cooling to 623 to 723 K, where isothermal treatment gave a bainitic microstructure. Dilatometric study of the same alloys showed that, during rapid cooling from the intercritical annealing temperature, about 30 pct of the austenite converted to epitaxial ferrite, which occurs under the PE condition. We have simulated this growth process using DICTRA.

Like the previous example, to stimulate PE-α/PE-γ growth using DICTRA, we have rewritten the Gibbs-energy and mobility data files for the α and γ phases in a generalized manner, so that the PE phase-diagram calculation and the growth simulation can be readily performed for any given composition in the Fe-Al-C-Mn-Si system. Unlike the previous example, the diffusion of C in both phases was considered. Then, the governing mass-conservation and flux equations under the PE condition are similar to Eqs. [27] and [28], respectively and the moving velocity of the PE-α/PE-γ interface is given by

$$\nu_\xi^{PE} = \frac{J_C^{\xi\alpha} - J_C^{\xi\gamma}}{X_C^{\xi\alpha} - X_C^{\xi\gamma}} \qquad [29]$$

Figure 10 shows the PE phase diagram, involving ferrite (PE-α) and austenite (PE-γ), for the Fe-0.05Al-xC-1.22Mn-1.52Si alloy. For the alloy C content of 0.26 mass pct and an intercritical annealing temperature of 1043 K, the phase fractions of PE-α and PE-γ are 0.42 and 0.58, respectively. Consistent with these phase fractions and the microstructural length scales,[37] we take a PE-α cell of 4 μm and a PE-γ cell of 5.52 μm for diffusional simulation in DICTRA. The initial C contents in these cells correspond to those given by the PE phase diagram at 1043 K, and these are labeled as $X_C^{PE-\alpha}$ and $X_C^{PE-\gamma}$ in Figure 10. Once again, we consider a flat geometry because the morphology of the epitaxial ferrite was a plate type rather than equiaxed.[37] The simulated results of PE-α growth at a constant cooling rate of 40 K/s from 1043 to 673 K are shown in Figure 11 as a function of time. It may be noted that about 40 pct of the original austenite pool has been converted to PE-α at the end of the
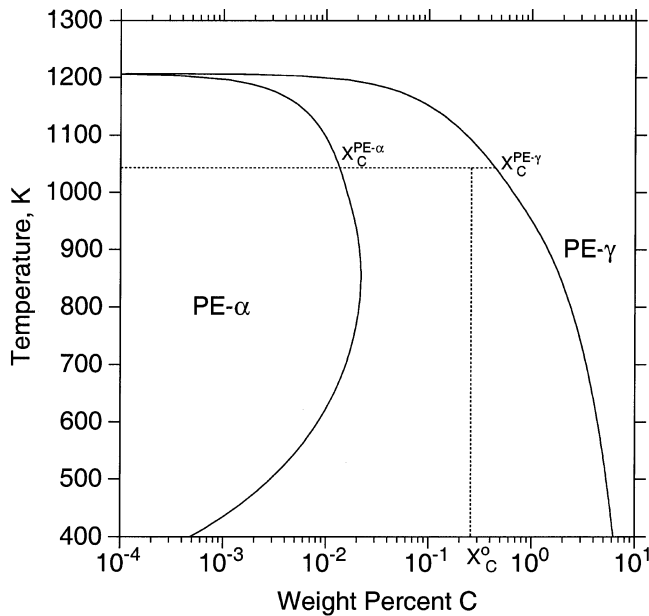
Fig. 10—The paraequilibrium phase diagram involving ferrite (PE-α) and austenite (PE-γ) for an Fe-0.05Al-xC-0.26C-1.22Mn-1.52Si alloy. The initial carbon content in the alloy is X_C^0, and the C contents in PE-α and PE-γ at 1043 K are marked as $X_C^{PE-\alpha}$ and $X_C^{PE-\gamma}$, respectively.

Fig. 11—The simulated paraequilibrium growth of PE-α having a flat interface with PE-γ in an Fe-0.05Al-0.26C-1.22Mn-1.52Si alloy as a function of time. The simulation was performed at a constant cooling rate of 40 K/s from 1043 to 673 K.

cooling period. This is in good agreement with the dilatometric results of Brandt,[37] who reported about 30 pct conversion. A higher predicted conversion may be due to the fact that dissipative force(s) was not considered in the calculation. As the PE-γ to PE-α reconstructive transformation takes place, the C content in PE-α initially increases with time (or with decreasing temperature) and then decreases. This is due the retrograde nature of C solubility in PE-α as shown in Figure 10. This, along with the decreasing diffusivity at lower temperatures, causes the development of the C profile within PE-α. On the other hand, due to the much slower diffusivity of C in austenite, a strong concentration profile develops near the transforming interface in PE-γ, and the far-field C profile remains the same as the initial profile.

In an Fe-0.05Al-0.26C-1.22Mn-1.58Si alloy, Brandt[37] observed an incubation time of 40 seconds at 673 K before the start of bainitic transformation. During the isothermal holding at 673 K and prior to the start of the bainitic transformation, two processes may take place: (1) continuation of the PE-γ to PE-α reconstructive transformation to reach their equilibrium volume fractions under the PE mode, and (2) homogenization of C distributions within PE-α and PE-γ. The results of the simulations of these processes are shown in Figure 12, where the dotted line is the C profile immediately after cooling from 1043 K. It is seen that PE-α has grown significantly during 40 seconds of isothermal hold. Even though the C profile within PE-α has changed, it is still not uniform. Once again, due to a much slower diffusivity of C in austenite, the C profile within PE-γ has broadened only marginally.

Figure 13 shows the relative volume fraction *vs* the simulated distribution of C within PE-γ at 673 K. In the low-alloy steels considered here, the stability of retained austenite against the martensitic transformation is primarily governed by its C content and the size of the austenite pool. In an Fe-0.05Al-0.26C-1.22Mn-1.58Si alloy that was intercritically
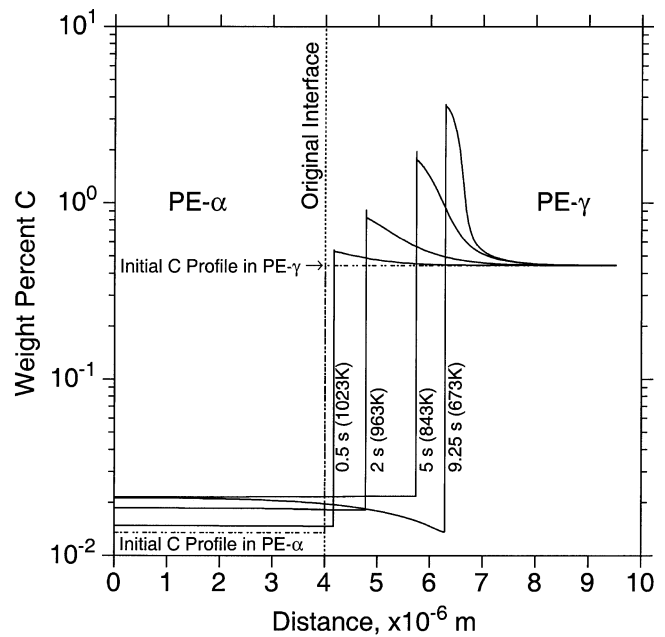
annealed at 1043 K and quenched, Brandt[37] found that the average C content in the retained austenite was about 1.36 mass pct as derived from the lattice-parameter measurements by X-ray diffraction. It is important to realize that, in the presence of a C profile, a part of the austenite pool that is least stable may transform to martensite during the final quench to room temperature. Based on the C profiles shown in Figure 13, we make three levels of estimates of the average C content in the austenite. First, we assume that PE-γ does not transform to martensite at all during the final quench; then, the average C contents in PE-γ are 0.499 and 0.774 mass pct, corresponding to the profiles at $t = 0$ and 40 s, respectively. This is an absolute lower-bound estimate. Second, we assume that the regions containing up to 0.444 mass pct C transform to martensite. According to our heterogeneous martensite nucleation kinetics model,[42,43] these regions will have an M_s temperature of 573 K or above. Due to sufficiently high M_s temperatures, these regions are expected to transform fully upon quenching to room temperature. Then the average C contents in PE-γ are 1.357 and 1.554 mass pct corresponding to the profiles at $t = 0$ and 40 s, respectively. Third, our model predicts that the regions with a C content of 1.47 mass pct will have an M_s of 300 K. However, all regions containing 1.47 mass pct or less C may not transform completely upon quenching to room temperature. A better criterion may be the C content that will give 90 pct transformation.[44] This was estimated to be 0.8 mass pct C. Then, the average C contents in PE-γ are 1.754 and 1.957 mass pct, corresponding to the profiles at $t = 0$ and 40 s, respectively. It may be noted that the measured[37] average C content of 1.36 mass pct is closer to our second method of estimation. This is due to the fact that, on one hand, it is unlikely (due to the very high M_s temperature) that there will be no martensitic transformation, as assumed in the first method and that, on the other hand, our third method of estimation is based on the transformation
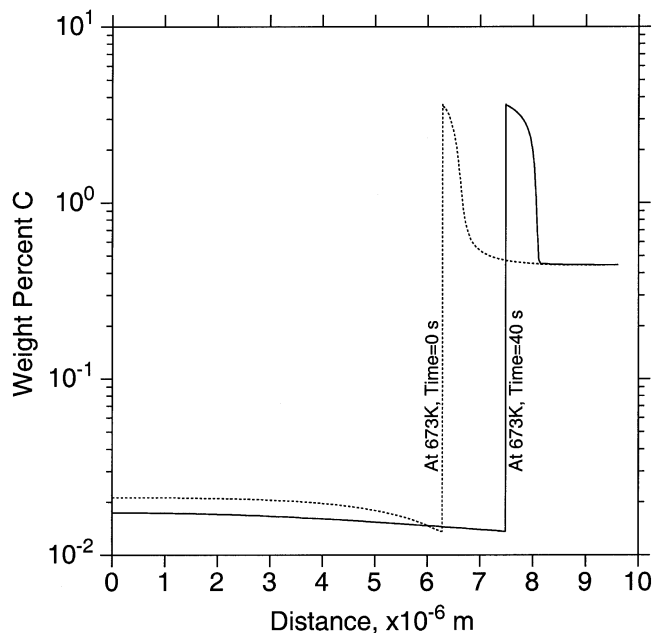
Fig. 12—The simulated paraequilibrium growth of PE-α at 673 K for 40 s. The isothermal holding for 40 s, but prior to the start of bainitic transformation, causes further growth of PE-α and homogenization of C, which is quite substantial within PE-α but only limited within PE-γ.

Fig. 13—The relative volume fraction of PE-γ and its C distribution at 673 K in an Fe-0.05Al-0.26C-1.22Mn-1.52Si alloy. The calculated average C contents by three methods (refer to text): (*a*) those immediately after quenching to 673 K are marked as C^I_0, C^{II}_0, and C^{III}_0, and (*b*) those after 40 s at 673 K are marked as C^I_{40}, C^{II}_{40}, and C^{III}_{40}. The measured[37] average C content in retained austenite is also shown by an arrow.

kinetics in the bulk samples,[44] which may be different in small (or finite-size) austenite pools, where the extent of transformation will be much less than in the bulk samples. Further systematic experimental measurements will certainly help develop kinetic models and tools for designing triple-phase steels containing PE-γ with an optimum stability. The needed critical information is the distribution of C and other solute elements within austenite and the size of the austenite pools.

In both case studies, we have considered the simplest form of a PE growth simulation. It was assumed that the PE mode prevails at nucleation and throughout the growth process and that no intermediate thermodynamic and/or kinetic state exists. In the case of PE-θ growth, this assumption was justified by the fact that the atomic-scale chemical analysis[19,27] did not reveal the presence of any compositional spike at the PE-α/PE-θ interface. We did not consider any dissipative forces, such as the interfacial energy, solute drag (with respect to C), finite interface mobility, *etc.*; as a result, the interface velocity obtained in the present analysis represents an upper limit. The relationship between these dissipative forces, the interface velocity, and the transition from one kinetic mode to another has been discussed extensively in the literature.[38–41] While we have treated the PE-θ transformation as a C diffusion–controlled precipitation process, there are some conflicting views in the literature regarding the classification of this phase transformation. At this time, there is no conclusive evidence of the role of shear, if any, on the growth kinetics of PE-θ, and when such evidence is available, it may be regarded as a coupled diffusional/displacive transformation.[39]

IV. CONCLUSIONS

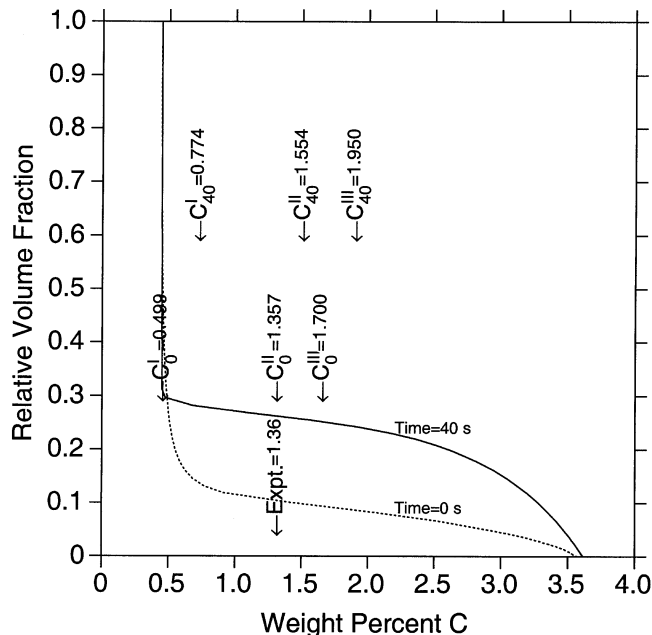A simple methodology is proposed to simulate PE growth in multicomponent systems using the current version of the

DICTRA software and database. The proposed methodology entails rewriting the Gibbs-energy and mobility data files for any given system and the phases of interest in such a manner that, for any given composition, the thermodynamic and mobility parameters of the hypothetical element Z can be readily obtained by knowing only the site fraction of the substitutional alloying elements in that system. A further advantage of the proposed methodology is that the PE phase diagrams of multicomponent systems can be constructed directly in conjunction with the POLY__3 module of Thermo-Calc software, which is otherwise not possible.

The results of the simulation of the growth of a cementite particle under PE with the lath martensitic matrix are presented for an Fe-0.247C-16.08Co-0.71Cr-2.82Mo-4.97Ni alloy. It is shown that once nucleated, the growth of PE cementite determined by C diffusion alone will be rather fast. Even though we did not consider any resistive force, the growth simulation of a simple diffusion geometry yields results that are in good agreement with the thickness of experimentally observed cementite particles. The estimated growth velocity from the experimental data also agree very well with the predicted growth velocity at a comparable size scale. The apparent deviation from the initial parabolic growth kinetics is attributed to a time-dependent rate constant.

The simulation of the growth of a ferrite particle into an austenite particle under the PE condition was also performed for an Fe-0.05Al-0.26C-1.22Mn-1.58Si alloy that was cooled at a constant rate of 40 K/s from 1043 to 673 K. The extent of ferrite growth by the end of the cooling period was found to be in good agreement with that derived from the dilatometry data. The calculated average C content in retained austenite was in reasonable agreement with that

derived from the lattice-parameter measurement by X-ray diffraction.

REFERENCES

1. A. Hultgren: *Trans. ASM*, 1947, vol. 39, pp. 915-1005.
2. M. Hillert: "Paraequilibrium", Internal Report, Swedish Institute for Metals Research, Stockholm, 1953.
3. J.S. Kirkaldy: *Can J. Phys.*, 1958, vol. 36, pp. 899-925.
4. G.R. Purdy, D.H. Weichert, and J.S. Kirkaldy: *Trans. AIME*, 1964, vol. 230, pp. 1025-34.
5. H.I. Aaronson, H.A. Domian, and G.M. Pound: *Trans. AIME*, 1966, vol. 236, pp. 768-81.
6. G.R. Purdy and M. Hillert: *Acta Metall.*, 1984, vol. 32, pp. 823-28.
7. H.K.D.H. Bhadeshia: *Progr. Mater. Sci.*, 1985, vol. 29, pp. 321-86.
8. M. Hillert and L.-I. Staffansson: *Acta Chem. Scand.*, 1970, vol. 24, pp. 3618-26.
9. M.J. Aziz: *J. Appl. Phys.*, 1982, vol. 53, pp. 1158-68.
10. A.J. Allen, D. Gavillet, and J.R. Weertman: *Acta Metall. Mater.*, 1992, vol. 41, pp. 1869-84.
11. J.S. Montgomery and G.B. Olson: *Proc. 34th Army Sagamore Conf. on Innovations in Ultrahigh-Strength Steel in Technology*, 1987, M. Azrin, G.B. Olson, and E.S. Wright, eds., U.S. Government Printing Office, Washington, DC, 1990, pp. 147-78.
12. G.B. Olson, T.J. Kinkus, and J.S. Montgomery: *Surface Sci.*, 1991, vol. 246, pp. 238-45.
13. T.J. Kinkus and G.B. Olson: *Surface Sci.*, 1992, vol. 266, pp. 391-96.
14. G. Ghosh, C.E. Campbell, and G.B. Olson: *Metall. Mater. Trans. A*, 1999, vol. 30A, pp. 501-12.
15. A. Umantsev and G.B. Olson: *Scripta Metall.*, 1993, vol. 29, pp. 1135-40.
16. C.E. Campbell: Ph.D. Thesis, Northwestern University, Evanston, IL, 1997.
17. B. Sundman, B. Jansson, and J.O. Andersson: *CALPHAD*, 1985, vol. 9, pp. 153-90.
18. A. Borgenstam, A. Engström, L. Höglund, and J. Ågren: *J. Phase Equilibria*, 2000, vol. 21, pp. 269-80.
19. R. Thomson and M.K. Miller: *Acta Metall.*, 1998, vol. 46, pp. 2203-13.
20. C. Wert: *Phys. Rev.*, 1950, vol. 79, pp. 601-05.
21. A.W. Bowen and G.M. Leak: *Metall. Trans.*, 1970, vol. 1, pp. 1695-1700.
22. A.T. Davenport and R.W.K. Honeycombe: *Met. Sci.*, 1975, vol. 9, pp. 201-08.
23. *Smithells Metals Reference Book*, 7th ed., E.A. Brandes and G.B. Brook, eds., Butterworth-Heinemann Ltd., Oxford, United Kingdom, 1992, pp. 13-20.
24. DICTRA, Version 20, Foundation of Computational Thermodynamics, Royal Institute of Technology, Stockholm, 1999.
25. R.G. Baker and J. Nutting: *J. Iron Steel Inst.*, 1959, vol. 192, pp. 257-68.
26. J. Chance and N. Ridley: *Metall. Trans. A*, 1981, vol. 12A, pp. 1205-13.
27. S.S. Babu, K. Hono, and T. Sakurai: *Metal. Mater. Trans. A*, 1994, vol. 25A, pp. 499-508.
28. B. Sundman and J. Ågren: *J. Phys. Chem. Solids*, 1985, vol. 42, pp. 297-301.
29. O. Redlich and A. Kister: *Ind. Eng. Chem.*, 1948, vol. 40, pp. 345-48.
30. M. Hillert and M. Jarl: *CALPHAD*, 1978, vol. 2, 227-38.
31. Solution Database, Scientific Group Thermodata Europe, Stockholm, 1994.
32. "Thermo-Calc, version M," Foundation of Computational Thermodynamics, Royal Institute of Technology, Stockholm, 1998.
33. R.-H. Liarng: Ph.D. Thesis, Northwestern University, Evanston, IL, 1996.
34. C. Knepfler: Ph.D. Thesis, Northwestern University, Evanston, IL, 1994.
35. J.-O. Andersson and J. Ågren: *J. Appl. Phys.*, 1992, vol. 72, pp. 1350-55.
36. G.R. Speich, V.A. Demarest, and R.L. Miller: *Metall. Trans. A*, 1981, vol. 12A, pp. 1419-28.
37. M.L. Brandt: Ph.D. Thesis, Northwestern University, Evanston, IL, 1997.
38. M. Hillert: *The Mechanism of Phase Transformations in Crystalline Solids*, The Institute of Metals, London, 1969, pp. 231-47.
39. G.B. Olson, H.K.D.H. Bhadeshia, and M. Cohen: *Acta Metall.*, 1989, vol. 37, pp. 381-89.
40. Z.-K. Liu and J. Ågren: *Acta Metall.*, 1989, vol. 37, pp. 3157-63.
41. G.R. Purdy and Y.J.M. Brechet: *Acta Metall. Mater.*, 1995, vol. 43, pp. 3763-74.
42. G. Ghosh and G.B. Olson: *Acta Metall. Mater.*, 1994, vol. 42, pp. 3361-70.
43. G. Ghosh and G.B. Olson: *Acta Metall. Mater.*, 1994, vol. 42, pp. 3371-79.
44. G. Ghosh and G.B. Olson: Research in Progress, Northwestern University, Evanston, IL, 2000.